Multi-material diffuse-interface Eulerian formulation for high-order simulations of elastic-plastic flow in solids

By N. S. Ghaisas, A. Subramaniam AND S. K. Lele

1. Motivation and objectives

Solids undergoing large deformations in contact with fluids occur in several engineering contexts including several manufacturing processes and processes involving cavitation. Robust and accurate handling of the interface between materials is the primary challenge encountered in numerical simulations of such phenomena. Lagrangian or Arbitrary Lagrangian-Eulerian (ALE) methods, where the mesh distorts with the motion of the interface, often fail when dealing with problems involving large deformations. Eulerian methods, on the other hand, are attractive since they employ fixed grids that do not deform with the motion and are not susceptible to failure due to mesh entanglement. They are also ideally suited for problems involving wave propagation and flow-like behavior. However, tracking the interface between materials becomes more complicated and requires a more careful treatment.

The motion of a single solid undergoing non-linear, elastic-plastic deformations can be tracked using the fully Eulerian framework introduced by Plohr & Sharp (1989, 1992). Several improvements to the formulation, advantageous from the perspective of numerical solution, were suggested by Trangenstein & Colella (1991) and Miller & Colella (2001). These latter formulations rely on the inverse deformation gradient tensor as the fundamental kinematic variable for tracking deformations of the solid. The constitutive behavior of solids is described by hyperelastic equations of state that maintain thermodynamic consistency. Extensions of this Eulerian framework to multiple materials follow either the sharp-interface methodology (Hill *et al.* 2010; Barton *et al.* 2013; López Ortega *et al.* 2014), or the diffuse-interface approximation (Favrie & Gavrilyuk 2012; Ndanou *et al.* 2015). The sharp-interface approach is most often used with level-set methods (Barton *et al.* 2013; López Ortega *et al.* 2014). Such an approach keeps the interface sharp and Reimann solvers or ghost-cells for the interface jump conditions can be used with relative ease. However, these methods leak mass since they are non-conservative and also tend to be excessively dissipative at the interface. Diffuse-interface approaches, on the other hand, do not preserve a sharp interface but smear it over a few grid points. They also require an explicit mixture treatment since there are a few numerically mixed cells close to the interface. They are, however, conservative and can be used with low dissipation schemes unlike the sharp-interface approach.

In addition to handling material interfaces, the capability to handle shocks and contact discontinuities is required in simulations of compressible solids and fluids. Most previous work has focused on implicitly adding the required dissipation in order to capture shocks and material interfaces. Ndanou *et al.* (2015) employ a Godunov-type scheme, for numerical solution of the diffuse-interface multi-material formulation, which is first-order accurate. The hybrid central difference - WENO scheme employed by López Ortega

et al. (2014), while formally third-order accurate, introduces upwinding and significant numerical dissipation. An alternative methodology for capturing shocks and interfaces in fluids (mainly ideal gases) was proposed and developed by Cook (2007, 2009) and Kawai *et al.* (2010), and combines high-resolution central compact finite-difference schemes (Lele 1992) with explicitly added numerical dissipation for numerical regularization. This Localized Artificial Diffusivity (LAD) scheme was extended and shown to be successful in capturing shocks in a single compressible material spanning the entire range of continuum models (from gases, liquids to elastic-plastic solids) in a unified manner, in our recent work (Ghaisas *et al.* 2016). The objective of the present document is to further extend the LAD scheme to interactions of shocks with multi-material interfaces, particularly between solids undergoing elastic-plastic deformations.

The mathematical formulation and the numerical solution procedure are discussed in the next section. The diffuse-interface multi-material model is used, since it assumes that a mixture of materials exists at every point in the computational domain, and it is suitable for use with global numerical schemes such as high-order compact finite differences. One-dimensional test problems that establish order of accuracy of the code are discussed, followed by a two-dimensional demonstration problem involving interaction between a shock and a perturbed interface between copper and aluminum. The document ends with a brief summary and comments about future work.

2. Numerical methodology

2.1. *Governing equations*

The fundamental equations governing motion of a multi-material continuum in Eulerian form are the mass, momentum and energy equations shown in index notation below:

$$\frac{\partial \rho Y_m}{\partial t} + \frac{\partial \rho Y_m u_k}{\partial x_k} = -\frac{\partial (J_m^*)_i}{\partial x_i}, \tag{2.1}$$

$$\frac{\partial \rho u_i}{\partial t} + \frac{\partial}{\partial x_k}\left[\rho u_i u_k - \sigma_{ik}\right] = \frac{\partial \tau_{ik}^*}{\partial x_k}, \tag{2.2}$$

$$\frac{\partial}{\partial t}\left[\rho\left(\varepsilon + \frac{1}{2}u_j u_j\right)\right] + \frac{\partial}{\partial x_k}\left[\rho u_k\left(\varepsilon + \frac{1}{2}u_j u_j\right) - \sigma_{ik}u_i\right] = \frac{\partial}{\partial x_k}\left[\tau_{ik}^* u_i - q_k^*\right], \tag{2.3}$$

where $\boldsymbol{u}$ is the velocity, and Y_m is the mass fraction of material m. ρ, ε and $\underline{\boldsymbol{\sigma}}$ are the mixture density, internal energy and Cauchy stress, respectively, given in terms of species-specific quantities ρ_m, ε_m and $\underline{\boldsymbol{\sigma}}_m$, by

$$\rho = \sum_{m=1}^{M} \alpha_m \rho_m, \quad \varepsilon = \sum_{m=1}^{M} Y_m \varepsilon_m, \quad \underline{\boldsymbol{\sigma}} = \sum_{m=1}^{M} \alpha_m \underline{\boldsymbol{\sigma}}_m, \tag{2.4}$$

where α_m is the volume fraction of material m and M is the total number of materials. $\underline{\boldsymbol{\tau}}^*$, $\boldsymbol{q}^*$ and $\boldsymbol{J}_m^*$ are the artificial viscous stress, artificial conductive flux and artificial diffusive flux described in Section 2.3.

These equations need to be supplemented with kinematic equations that track the deformation of the material that is required to compute the Cauchy stress in each material. Deformations of a material are tracked in terms of the inverse deformation gradient tensor $\underline{\boldsymbol{g}}$ defined as

$$\underline{\boldsymbol{g}} = \partial \boldsymbol{X} / \partial \boldsymbol{x}, \tag{2.5}$$

where $\boldsymbol{x}$ is the position of a continuum parcel in the deformed state (Eulerian coordinate in this case) and $\boldsymbol{X}$ is the position of the parcel in the reference state.

A multiplicative decomposition of the inverse deformation gradient tensor is assumed as in Miller & Colella (2001), $\underline{\boldsymbol{g}} = \underline{\boldsymbol{g}}^p \underline{\boldsymbol{g}}^e$, such that $\underline{\boldsymbol{g}}^e$ tracks the elastic component of the total inverse deformation gradient tensor while $\underline{\boldsymbol{g}}^p$ tracks the plastic component of the inverse deformation gradient tensor. To track the deformations in the solid medium, we solve for only the elastic part of the inverse deformation gradient tensor $\underline{\boldsymbol{g}}^e$, and model the effect of plasticity. The equations governing the evolution of the elastic part of the inverse deformation gradient tensor for material m, $\underline{\boldsymbol{g}}^e_m$ can be written as in López Ortega *et al.* (2014) and Ndanou *et al.* (2015)

$$\frac{\partial (g^e_m)_{ij}}{\partial t} + \frac{\partial u_k (g^e_m)_{ik}}{\partial x_j} = u_k \left(\frac{\partial (g^e_m)_{ik}}{\partial x_j} - \frac{\partial (g^e_m)_{ij}}{\partial x_k} \right) + \zeta_g \left(\frac{\rho_m}{\rho_{0,m} |\underline{\boldsymbol{g}}_m|} - 1 \right) (g^e_m)_{ij} + \frac{1}{2\mu_m \left(\frac{\rho_m}{\rho_{0,m}} \right) \tau_{0,m}} \left[\frac{\mathrm{H}\left(||\underline{\boldsymbol{\sigma}}'_m||^2 - \frac{2}{3}\sigma^2_{Y,m} \right)}{\mu^2_m} \right] (g^e_m)_{ik} \, \sigma'_{kj}. \tag{2.6}$$

The second term on the right hand side is to ensure consistency with the material density and $\zeta_g = 1/(6\Delta t)$ is a time step dependent constant based on stability considerations. The last term on the right-hand side of Eq. (2.6) accounts for plasticity effects where, μ_m denotes the shear modulus, $\rho_{0,m}$, density in the undeformed state, $\sigma_{Y,m}$ is the yield stress and $1/\tau_{0,m}$, an inverse relaxation time scale of material m. $\underline{\boldsymbol{\sigma}}'$ denotes the deviatoric part of the tensor $\underline{\boldsymbol{\sigma}}$. The Heaviside function, H(), turns off plasticity effects whenever the yield criterion $||\underline{\boldsymbol{\sigma}}'_m||^2 = \underline{\boldsymbol{\sigma}}'_m : \underline{\boldsymbol{\sigma}}'_m = \sigma'_{ij,m}\sigma'_{ij,m} < \frac{2}{3}\sigma^2_{Y,m}$.

2.1.1. *p-T equilibrium*

In addition to the Eqs. (2.1)-(2.3) and (2.6), we require two more equations per material apart from the equation of state to close the system. One approach is to solve the volume fraction and species energy equations to close the system. We have found that this approach is not very robust, and maintaining thermodynamic consistency requires a more sophisticated treatment of the volume fraction equation that includes dissipation terms corresponding to the artificial diffusive fluxes. A different approach is to assume pressure and temperature equilibrium between different materials present in one grid cell. This assumption is justified if the pressure and temperature relaxation time scales are much smaller than the flow time scales. With this assumption, for a total of M species we have

$$p = p_1 = p_2 = \cdots = p_M, \tag{2.7}$$

$$T = T_1 = T_2 = \cdots = T_M, \tag{2.8}$$

$$\sum_{m=1}^{M} \alpha_m = 1, \quad \sum_{m=1}^{M} Y_m \varepsilon_m = \varepsilon, \quad \varepsilon_m = \varepsilon_m \left(\rho_m, p_m, \underline{\boldsymbol{g}}^e_m \right), \tag{2.9}$$

which is a system of $2M+2$ non-linear equations that is solved for the $2M+2$ unknowns, p, T, α_m and ε_m after each stage of the time-advancement stage. This method is an extension of a similar procedure described by Cook (2009), for ideal gases, to the current system involving elastic-plastic solids.

2.2. *Constitutive description*

An equation of state (EOS) is required to close the above system of equations. In this study, we consider a classical hyperelastic form of the EOS, without additional contributions due to capillary/Korteweg effects. The stress is derived from an energy functional based on thermodynamic consistency. The constitutive description used here is the same as that of Favrie & Gavrilyuk (2012). We consider an additive split of the internal energy ε_m into a volumetric (or hydrodynamic) component ε_m^h and an isochoric (or elastic) component ε_m^e as in Ndanou *et al.* (2015).

$$\varepsilon_m = \varepsilon_m^h(p, \rho_m) + \varepsilon_m^e(\underline{\boldsymbol{g}}_m^e). \tag{2.10}$$

The specific expression for the hydrodynamic part of internal energy used in this study is analogous to a stiffened gas and is given by

$$\varepsilon_m^h = \frac{p + \gamma_m p_{\infty,m}}{(\gamma_m - 1)\rho_m}, \tag{2.11}$$

where $p_{\infty,m}$ (with units of pressure) and γ_m (non-dimensional) are material constants.

The dependence of the elastic component of the internal energy on the deformations can be expressed in many different ways. In this study, the expression is taken to be

$$\varepsilon_m^e = \frac{\mu_m}{4\rho_{0,m}} tr\left(\left(\hat{\underline{\boldsymbol{g}}}_m - \underline{\boldsymbol{I}}\right)^2\right), \tag{2.12}$$

where μ_m and $\rho_{0,m}$ are the shear modulus and density in the undeformed state, respectively, and $\hat{\underline{\boldsymbol{g}}}_m = |\underline{\boldsymbol{G}}_m^e|^{-1/3}\underline{\boldsymbol{G}}_m^e$, with $\underline{\boldsymbol{G}}_m^e = \left(\underline{\boldsymbol{g}}_m^e\right)^T \underline{\boldsymbol{g}}_m^e$, and $|\underline{\boldsymbol{G}}_m^e|$ denotes the determinant of $\underline{\boldsymbol{G}}_m^e$.

With this separable form of the EOS as described above, the Cauchy stress of material m satisfying the Clausius-Duhem inequality (enforcing consistency with the second law of thermodynamics) can be written out analytically as

$$\underline{\boldsymbol{\sigma}}_m = -p\underline{\boldsymbol{I}} - \mu_m \frac{\rho_m}{\rho_{0,m}}\left(|\underline{\boldsymbol{G}}_m^e|^{-2/3}\mathrm{dev}\left((\underline{\boldsymbol{G}}_m^e)^2\right) - |\underline{\boldsymbol{G}}_m^e|^{-1/3}\mathrm{dev}\left(\underline{\boldsymbol{G}}_m^e\right)\right), \tag{2.13}$$

where $\mathrm{dev}(\underline{\boldsymbol{G}}^e)$ denotes the deviatoric part of $\underline{\boldsymbol{G}}^e$.

2.3. *Numerical solution procedure*

We solve the set of Eqs. (2.1)-(2.6) on a fixed Eulerian structured grid using a tenth-order compact finite difference scheme (Lele 1992). A fourth-order 5-stage Runge-Kutta time integrator (Kennedy *et al.* 2000) is used. After each stage, the conserved variables are filtered for de-aliasing using an 8^{th} order compact filter (Lele 1992). Compact finite difference schemes provide spectral-like resolution capabilities but are much more flexible than spectral schemes. The centered schemes used here have no inherent dissipation. Dissipation required for shock and interface capturing is added explicitly and is described in Section 2.3.1.

2.3.1. *Shock and interface capturing*

Since we wish to decouple the dissipation required to capture shocks and interfaces from the underlying numerical scheme, we use the LAD method as in Ghaisas *et al.* (2016). Here, we extend the LAD method to the multi-material elastic-plastic formulation following the original LAD scheme of Cook (2007). The main idea is to add an artificial

viscous stress, artificial heat flux and artificial diffusive flux as numerical regularization in Eqs. 2.1 to 2.3. $\underline{\boldsymbol{\tau}}^*$ is the artificial viscous stress as in Ghaisas *et al.* (2016). $\boldsymbol{J}_m^*$ is the artificial diffusive flux given by

$$(J_m^*)_i = -\rho \left(D_m^* \frac{\partial Y_m}{\partial x_i} - Y_m \sum_k D_k^* \frac{\partial Y_k}{\partial x_i} \right), \tag{2.14}$$

where D_m^* is the diffusivity of species m given by

$$D_m^* = C_D c_s \overline{\left| \left(\sum_{i=1}^{3} \frac{\partial^r}{\partial x_i^r} Y_m \Delta_i^r \Delta_{i,Y} \right) \right|} + C_Y \overline{c_s \left(|Y_m| - 1 + |1 - Y_m| \right) \Delta_Y}. \tag{2.15}$$

$r = 4$ is used here and $\overline{f}$ indicated a truncated Gaussian filtered version of function f as in Cook (2007). c_s is the speed of sound in the mixture, Δ_i is the grid spacing in direction i and $\Delta_{i,Y}$ and Δ_Y are mass fraction-gradient weighted grid-length measures given by

$$\Delta_{i,Y} = \Delta_i \frac{\left(\frac{\partial Y_m}{\partial x_i} \right)^2}{\sum_{k=1}^{3} \left(\frac{\partial Y_m}{\partial x_k} \right)^2 + \epsilon}, \qquad \Delta_Y = \frac{\sum_{k=1}^{3} \Delta_k \left| \frac{\partial Y_m}{\partial x_k} \right|}{\sqrt{\sum_{k=1}^{3} \left(\frac{\partial Y_m}{\partial x_k} \right)^2}}, \tag{2.16}$$

and $\epsilon = 10^{-32}$ is a small constant to avoid division by zero.

$\boldsymbol{q}^*$ is the artificial heat conductive flux given by

$$q_i^* = q_i^{c,*} + q_i^{d,*}, \tag{2.17}$$

$$q_i^{c,*} = -\kappa^* \frac{\partial T}{\partial x_i}, \qquad q_i^{d,*} = \sum_{m=1}^{M} h_m (J_m^*)_i, \tag{2.18}$$

$$h_m = \varepsilon_m^h + \frac{p_m}{\rho_m}. \tag{2.19}$$

$\boldsymbol{q}^{d,*}$ is the enthalpy diffusion flux (Cook 2009) and h_m is the species enthalpy. The artificial conductivity κ^* is computed as in Ghaisas *et al.* (2016). The default values described in Ghaisas *et al.* (2016) and Cook (2007) are used for all LAD coefficients.

2.3.2. *Polar decomposition of* $\underline{\boldsymbol{g}}^e$

In problems involving large deformations, situations involving roll-up and reconnection of material interfaces may be expected. These situations pose a challenge to numerical simulations since the $\underline{\boldsymbol{g}}^e$ tensor may be discontinuous across the interface while the stress state is continuous. This problem arises since the formulation makes no attempt to recognize the isotropy of the materials involved. A solution to this problem proposed by López Ortega *et al.* (2014) is to use the polar decomposition of $\underline{\boldsymbol{g}}^e$. Consider

$$\underline{\boldsymbol{g}}^e = \underline{\boldsymbol{R}}\, \underline{\boldsymbol{v}}, \tag{2.20}$$

where $\underline{\boldsymbol{R}}$ is a rotation matrix and $\underline{\boldsymbol{v}}$ is symmetric and positive semi-definite. Since the internal energy and the Cauchy stress only depend on $\left(\underline{\boldsymbol{g}}^e\right)^T \underline{\boldsymbol{g}}^e = \underline{\boldsymbol{v}}^T \underline{\boldsymbol{v}}$, we can solve for $\underline{\boldsymbol{v}}$ instead that is continuous across an interface when the stress field is continuous. Equations for $\underline{\boldsymbol{R}}$ and $\underline{\boldsymbol{v}}$ can be derived from Eq. (2.5) as in López Ortega *et al.* (2014). The equation for $\underline{\boldsymbol{v}}$ is identical to that of $\underline{\boldsymbol{g}}^e$ and we do not need to track $\underline{\boldsymbol{R}}$. We need to ensure that $\underline{\boldsymbol{v}}$ is symmetric and positive semi-definite, which the equation does not

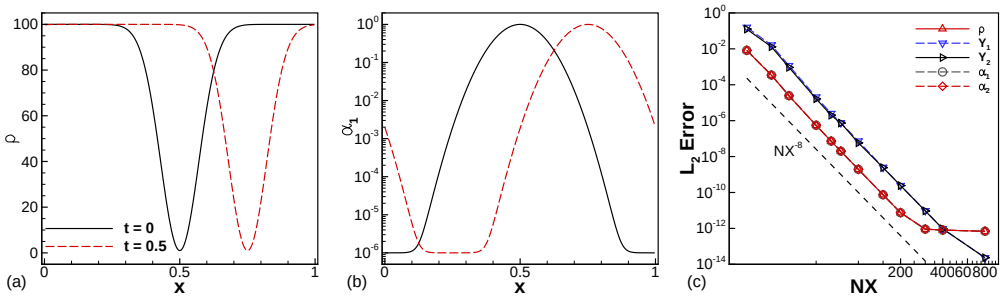

FIGURE 1. Advection of a mixture of materials with density ratio 100, described by a Gaussian pulse for one of the volume fractions. Spatial profiles at two time instants of (a) mixture density, (b) volume fraction of material 1 using $NX = 400$, $dt = 2.5 \times 10^{-4}$. (c) Spatial convergence test showing eighth-order accuracy in different species-specific quantities.

guarantee. Hence, after an update of all 9 components of $\underline{\boldsymbol{v}}$ from level n to $n+1$, we perform the polar decomposition and implicitly remove the rotation part of the updated tensor.

$$\underline{\tilde{\boldsymbol{v}}}^{n+1} \xleftarrow{\text{update}} \underline{\boldsymbol{v}}^{n}, \tag{2.21}$$

$$\underline{\boldsymbol{v}}^{n+1} = \sqrt{\left(\underline{\tilde{\boldsymbol{v}}}^{n+1}\right)^{T} \underline{\tilde{\boldsymbol{v}}}^{n+1}}. \tag{2.22}$$

3. Results

3.1. *Order of accuracy*

In order to establish the order of accuracy of the code, we consider advection of a smooth interface between two elastic solids on a periodic domain, $x \in [0, 1]$, with a velocity $u = 0.5$. The two solids have identical properties $\gamma_1 = \gamma_2 = 1.4$, $p_{\infty,1} = p_{\infty,2} = 1$, $\mu_1 = \mu_2 = 1$, $\sigma_{Y,1} = \sigma_{Y,2} = \infty$, except for the undeformed densities, which are taken to be $\rho_{0,1} = 1$, and $\rho_{0,2} = 100$. The properties have been non-dimensionalized with a pressure scale, $p_{\infty,1}$, a density scale, $\rho_{0,1}$, and a length scale equal to the domain length. The initial volume fraction of material 1 varies from α_{min} to $1 - \alpha_{min}$, $\alpha_{min} = 10^{-6}$, with a Gaussian profile centered at $x = 0.5$ and with standard deviation 0.1. Due to the advection of the material mixture, the Gaussian pulse is seen to be centered at $x = 0.75$ at $t = 0.5$ in Figures 1(a) and (b). Using the analytical solution of the advecting mixture, a convergence study is performed. Figure 1(c) shows that the errors in volume and mass fractions and mixture-density reduce at eighth order.

The second example considered consists of a linear plane-strain wave of infinitesimal strength crossing an interface between two materials with density ratio of 2. The material constants, non-dimensionalized using pressure and density scales $p_{\infty,1}$ and $\rho_{0,2}$ respectively, are $\gamma_1 = \gamma_2 = 1.4$, $p_{\infty,1} = p_{\infty,2} = 1$, $\mu_1 = \mu_2 = 0$, $\rho_{0,1} = 0.5$, and $\rho_{0,2} = 1$. The initial volume fractions are

$$\alpha_1 = \alpha_{min} + \frac{(1 - 2\alpha_{min})}{2}\left[\text{erf}\left(\frac{x - 0.5}{\delta_t \Delta x}\right) - \text{erf}\left(\frac{x - 0.9}{\delta_t \Delta x}\right)\right], \quad \alpha_2 = 1 - \alpha_1, \tag{3.1}$$

with $\alpha_{min} = 10^{-6}$. The parameter δ_t defines the numerical thickness of the interfaces at $x = 0.5$ and $x = 0.9$, the domain length is $L_x = 1$ and $\Delta x = L_x/NX$. Periodic boundary conditions are used while solving the problem. A compression wave with a Gaussian

profile and amplitude $\sigma_0 \ll 1$ is initalized at $x = 0.35$,

$$\sigma_{11} = -\sigma_0 e^{-((x-c_{L,1}t-0.35)/0.035)^2}, \tag{3.2}$$

$$\sigma_{22} = \sigma_{33} = \frac{\lambda_{L,1}}{\lambda_{L,1}+2\mu_{L,1}}\sigma_{11}, \quad u = -\frac{c_{L,1}}{(\lambda_{L,1}+2\mu_{L,1})}\sigma_{11}, \tag{3.3}$$

where

$$\mu_{L,i} = \mu_i, \quad \lambda_{L,i} = \gamma_1 p_{\infty,i} - 2\mu_i/3, \quad c_{L,i} = \sqrt{(\lambda_{L,i}+2\mu_{L,i})/\rho_{0,i}}. \tag{3.4}$$

are the equivalent Lamé coefficients (see, e.g., Achenbach (1975)) and the linear longitudinal wave speed in material i. The deformations in the two materials are initialized according to

$$g_{11,i} = \left[1 + \frac{\sigma_{11}}{(\lambda_{L,i}+2\mu_{L,i})}\right]^{-1}, \quad \rho_i = \rho_{0,i} g_{11,i}. \tag{3.5}$$

All other components of stress, inverse deformation gradient tensor and velocity are assumed to be trivial.

Interaction of the Gaussian pulse with the interface at $x = 0.5$ leads to a transmitted as well as a reflected pulse, as seen in Figures 2(a) and (b). The transmission and reflection coefficients, which determine the magnitudes of the respective waves, are given analytically in the case of a sharp interface by (Achenbach 1975) $C_{trans} = [2\rho_2 c_{L,2}/\rho_1 c_{L,1}] / [\rho_2 c_{L,2}/\rho_1 c_{L,1} + 1]$, $C_{refl} = [\rho_2 c_{L,2}/\rho_1 c_{L,1} - 1] / [\rho_2 c_{L,2}/\rho_1 c_{L,1} + 1]$.

Figure 2(c) compares the pressure profiles of the reflected wave obtained from the diffuse-interface approximation to the analytical solution corresponding to a sharp interface. For fixed NX, the numerical solution to the diffuse-interface approximation approaches the sharp-interface exact solution as the parameter δ_t is reduced. Error convergence rates are analyzed in Figure 2(c). A finite error is always present when comparing a diffuse-interface solution with the sharp-interface analytical solution, and hence, convergence at eighth order is not expected. Figure 2(d) shows that the errors in pressure with respect to the analytical solution reduce at fourth order. Taking a very finely resolved solution to the diffuse-interface model as the exact solution leads to convergence at sixth order. This is not consistent with the eighth-order numerical schemes employed, which suggests either the solution at $NX = 12800$ is not fully converged, or non-linear errors are significant enough to preclude eighth-order accuracy in the current test problem. Nevertheless, the method is seen to converge at a rate higher than second-order, which would be expected using previous lower order schemes.

3.2. *Problems with motion of solid-solid interfaces*

The ability to handle large property jumps is demonstrated in Figure 3. The materials are described by identical values for $\gamma = 1.4$, $p_\infty = 1$, $\mu = 1$, $\sigma_Y = \infty$, while the densities are $\rho_{0,1} = 1$, and $\rho_{0,2} = 1000\rho_{0,1}$. Simulations are conducted on a periodic 1D domain $x \in [0, 1]$, with an advection velocity $u = 0.5$. The initial volume fractions are given by Eq. (3.1) with $\delta_t = 2.5$, so as to smear the interface over 9 grid points using $NX = 401$. Figure 3 shows that the interface retains its sharpness even after one full advection time period. The volume fraction profiles plotted in logarithmic scale show some oscillations, but no negative volume fractions are encountered in these tests.

For evaluating the plastic algorithm and establishing the quantitative accuracy of our method, we consider the single material impact problem described in Favrie & Gavrilyuk (2011). The single material problem is simulated using our multi-material algorithm, by assigning identical parameter values to the two materials. The material properties are

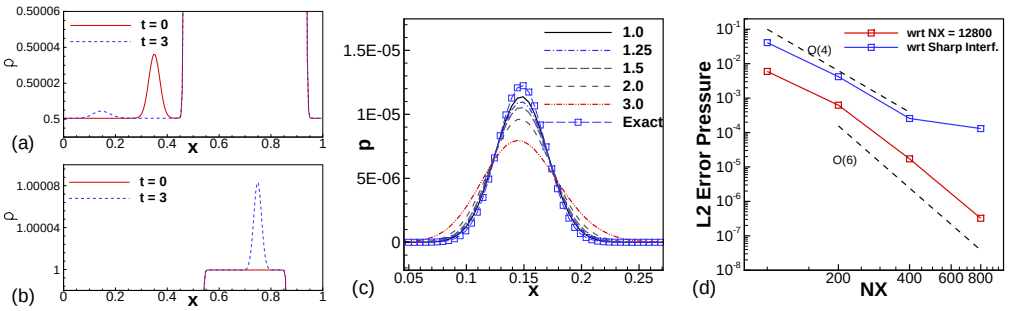

FIGURE 2. Interaction of a linear plane-strain wave with an interface of density ratio 2. Density profiles focusing on (a) initial and reflected waves, and (b) transmitted waves. (c) Pressure profiles of the reflected wave with fixed $NX = 200$, and varying δ_t denoted in the legend, (d) spatial convergence with fixed $\delta_t \Delta x = 0.001$.

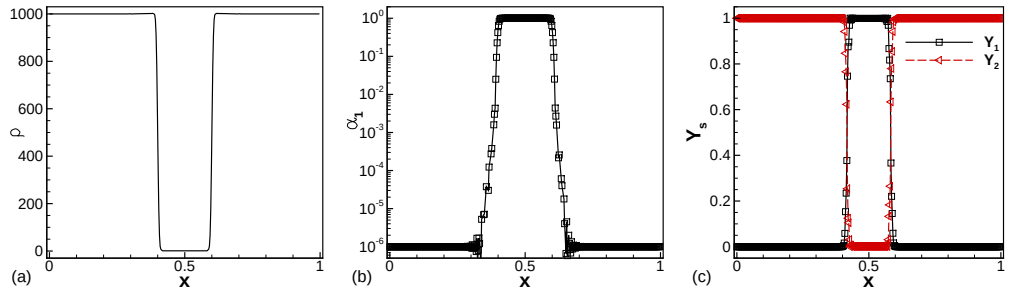

FIGURE 3. Advection of a material interface. Profiles after one time period, $t = 2$, of (a) mixture density, (b) volume fractions and (c) mass fractions for density ratio $R_\rho = \rho_{0,2}/\rho_{0,1} = 1000$. $NX = 401$ and $CFL = 0.8$ are used.

$\gamma_1 = \gamma_2 = 2.84$, $p_{\infty,1} = p_{\infty,2} = 0.6$ GPa, $\mu_1 = \mu_2 = 77$ GPa, $\sigma_{Y,1} = \sigma_{Y,2} = 2.49$ GPa, and $\rho_{0,1} = \rho_{0,2} = 7850$ kg/m^3. The solution at $t = 0.1$ ms is shown in Figure 4 using $NX = 401$ and $CFL = 0.8$. The density and velocity profiles agree well with the single material results of Favrie & Gavrilyuk (2011) for all three values of impact velocities. Similar to the reference results, only elastic waves are present in the ± 50 m/s impact case, while elastic precursor and plastic waves are present in the ± 150 m/s and ± 300 m/s impact cases.

3.3. *Shock-interface interaction*

Interaction of a shock wave with material interfaces is studied next. A material interface is initialized at $x = 0.5$ between solids described by $\gamma = 1.4$, $p_\infty = 1$, $\mu = 1$, $\sigma_Y = \infty$, while the densities are $\rho_{0,1} = 1$, and $\rho_{0,2} = R_\rho$. The ambient pressure is initialized to 0.1. A right-moving shock of pressure ratio 4 is initalized in material 1 at $x = 0.25$. Velocity and mixture-density profiles are shown in Figure 5 at $t \approx 0.27$ after the shock has crossed the interface for $R_\rho = 1$, 2 and 10. For $R_\rho = 1$, the shock wave crosses the material interface without generating spurious waves, since the two materials are identical in all respects, whereas transmitted and reflected waves are seen for $R_\rho = 2$ and 10.

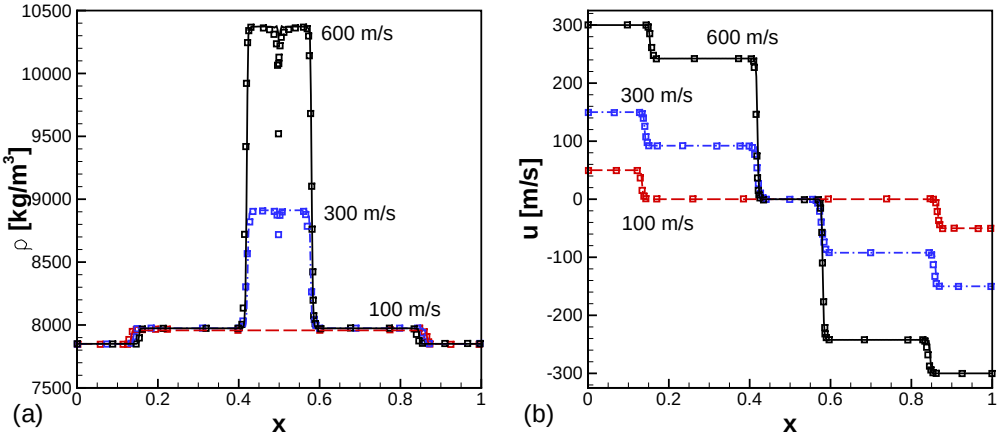

FIGURE 4. Single material impact problem solved using the multi-material algorithm at $t = 0.1$ ms using $NX = 401$, $CFL = 0.8$. (a) Density and (b) normal velocity profiles from current simulations (lines) compared to results in Favrie & Gavrilyuk (2011) (symbols). The impact velocities in the labels are the relative velocities between the two plates.

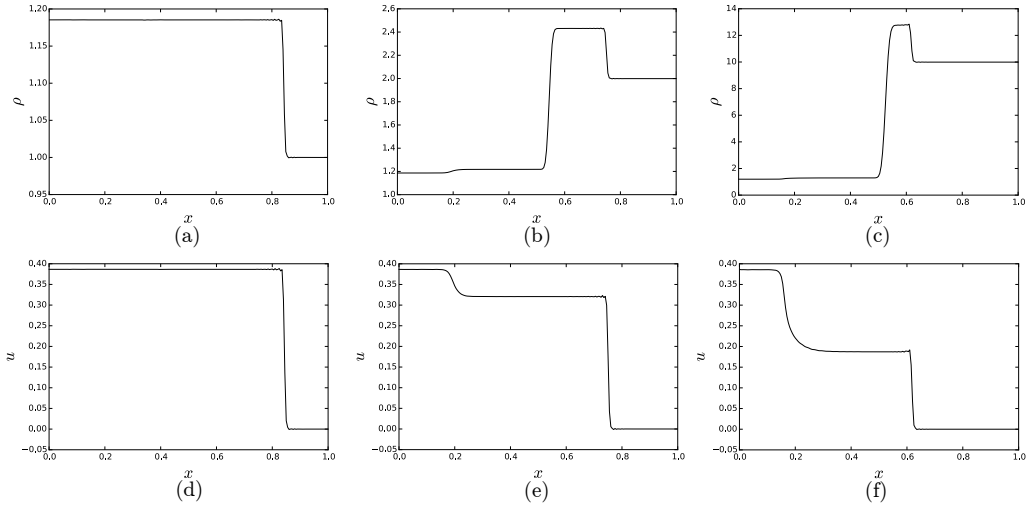

FIGURE 5. Shock interaction with a material interface between two solids. (a), (b) and (c) are the mixture-density for initial density ratios, $R_\rho = 1$, 2 and 10, respectively. (d), (e) and (f) are the velocity profiles for initial density ratios of 1, 2 and 10, respectively. Results at $t \approx 0.27$ using $NX = 201$ and $CFL = 0.8$.

3.4. *Richtmyer-Meshkov instability of a copper-aluminum interface*

A two-dimensional test involving interaction of a shock with an interface between copper (Cu) and aluminum (Al) is discussed. Copper is described by the material parameters $\gamma_1 = 2$, $p_{\infty,1} = 68.23$ GPa, $\mu_1 = 39.38$ GPa, $\rho_{0,1} = 8930$ kg/m^3, and $\sigma_{Y,1} = 0.12$ GPa. The EOS parameters for aluminum are $\gamma_2 = 2.088$, $p_{\infty,2} = 32.98$ GPa, $\mu_2 = 27.09$ GPa, $\rho_{0,2} = 2712$ kg/m^3, and $\sigma_{Y,2} = 0.297$ GPa. These parameter values are derived from the Godunov-Romenskii EOS parameters used for these metals and reported in López Ortega (2013). The parameter values used here ensure that the speed of sound of a linear wave

is equal to that with the Godunov-Romenskii EOS used by López Ortega (2013). All results are non-dimensionalized by a pressure scale $\gamma_1 p_{\infty,1}$ and density scale ρ_1.

The rectangular simulation domain extends from the point $(-2, 0)$ to $(4, 1)$ for lengths 6 and 1 in the x and y directions, respectively. A portion of the domain is seen in Figure 6(a). A numerical sponge layer, which absorbs outgoing waves and minimizes reflection, is applied at the left boundary, between $x = -2$ and $x = 0$, while a rigid wall is assumed at the right boundary, $x = 4$. The top and bottom boundaries are periodic. The interface is initialized at $x = 2$ with a single-mode sinusoidal perturbation,

$$\eta(x, y) = 2 + \eta_0 \sin(ky). \tag{3.6}$$

Following López Ortega (2013), the parameter $k = 4\pi$ is used, so that two full wavelengths are included in the domain, and the initial amplitude of perturbations is given by $\eta_0 k = 0.4$. A shock with pressure ratio of 25 is initiated in copper at $x = 1.5$, and is moving to the right towards the Cu-Al interface. An x-t diagram of the problem with a flat interface is shown in Figure 7(c).

Results of a simulation using 768×128 grid points are seen in Figure 6 and Figure 7. The initial density contours (Figure 6(a)) show the initial shock and material interface. The shock deposits vorticity on the material interface due to baroclinic torque. As suggested by the linear analysis of Plohr & Plohr (2005), the deposition of baroclinic vorticity renders the interface unstable. The propagating shocks are strong enough that the yield stresses of both, aluminum and copper, are exceeded, and both solids undergo plastic flow. The vorticity contours at $t = 1.0$ (see Figure 6(c)) indicate that, due to plastic flow, the bulk of the deposited vorticity is retained in the interfacial region, and only a small amount is carried away by weak elastic shear waves (not seen in the scale used for vorticity contours here). The density contours in Figure 6(b) show that the interface is set in motion towards the right and has undergone a phase reversal since the shock interacts with a heavy-light interface. The shock transmitted into aluminum rebounds from the rigid wall at the right boundary at $t \approx 0.98$. This reflected shock interacts with the disturbed interface a second time at $t \approx 1.4$, leading to a left-moving transmitted shock and a right-moving, weaker, reflected shock. The reflected shock rebounds from the rigid wall once again, and a series of re-shocks and interface interactions is set up, eventually halting the translation of the interface. Since most of the vorticity is retained at the interface due to plastic effects and only a small portion is transported out by elastic shear waves, the interface curls up and a large deformation of the interface is observed as in Figures 6(d) and (e), along with the characteristic shapes of the copper spikes and aluminum bubbles.

The initiation of motion, initial linear growth, and subsequent non-linear growth of the instability are seen in the x locations of the spikes and bubbles in Figure 7(a). The location of spikes is defined as the maximum x for which $Y_{Cu} > 0.5$, and the location of bubbles is defined as the minimum x for which $Y_{Cu} < 0.5$. The shock-interface interaction and ensuing interface instability are also seen in the evolution of integrated positive vorticity, $\Gamma^+ = \int \frac{\omega_z + |\omega_z|}{2} \mathrm{dxdy}$, where $\omega_z = (\partial u/\partial y - \partial v/\partial x)$.

The effect of grid resolution on the density contours is shown in Figure 8. As the grid is refined, more of the fine-scale structure of the interface is resolved. The location of shock waves in the domain is also seen to be the same across the different resolutions, a consequence of the fact that the formulation is fully conservative. Statistics plotted in Figure 7 are well converged before the first reshock at $t \approx 1.4$. After the first reshock, the differences between the $NY = 64$ and the $NY = 128$ simulation results are smaller than

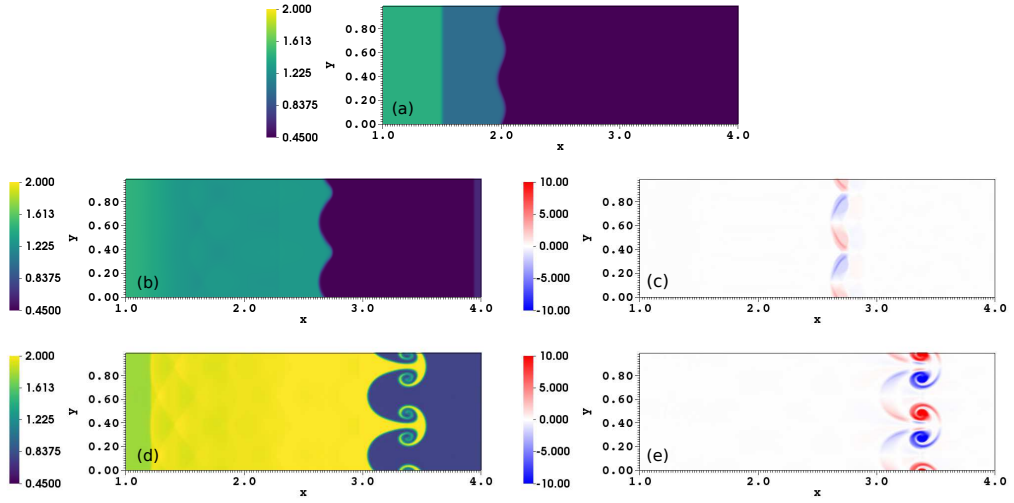

FIGURE 6. Density and vorticity contours in the Cu-Al RM problem with 128 points in the transverse direction. (a) initial mixture-density (b) density profile at $t = 1.0$ (c) vorticity profile at $t = 1.0$ (d) density profile at $t = 3$ (e) vorticity profile at $t = 3$.

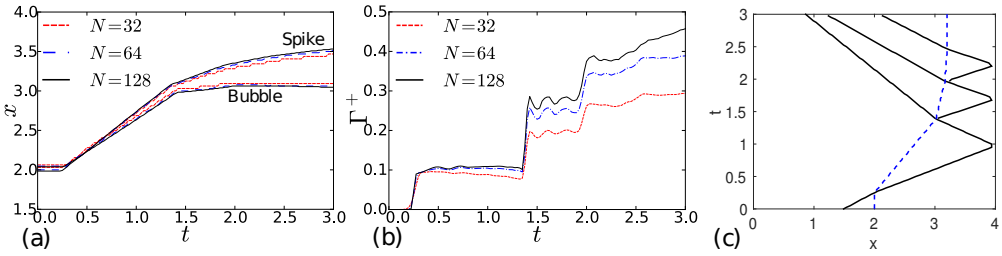

FIGURE 7. (a) Spike (upper set of lines) and bubble locations (lower set of lines) and (b) net integrated positive vorticity plotted for the three different grid resolutions. Number of points in the transverse direction are represented in the legend. (c) $x - t$ diagram showing evolution of shock (solid lines) and interface (dashed line) locations with time.

those between the $NY = 32$ and $NY = 64$ results. This indicates that simulations are approaching convergence, but are not fully converged on the 768×128 grid. Although an exact, fair, comparison is not possible due to the different EOSs employed to describe copper and aluminum, the results of López Ortega (2013) (see their Figures C.6 and C.9) suggest that effectively 1024 grid points in the y direction are required to resolve the features seen in Figure 8(c) using their numerical method.

4. Conclusions

The final aim of this work is to develop the capability for fully Eulerian, high-order simulations of elastic-plastic solid deformations, coupled with fluid flows. Towards this goal, a numerical framework, comprised of tenth-order compact finite-difference schemes and a localized artificial diffusivity shock-capturing method, is applied to a diffuse-interface multi-material formulation governing elastic-plastic deformations of solids. The order of accuracy and the ability to handle shocks and material interfaces are demonstrated

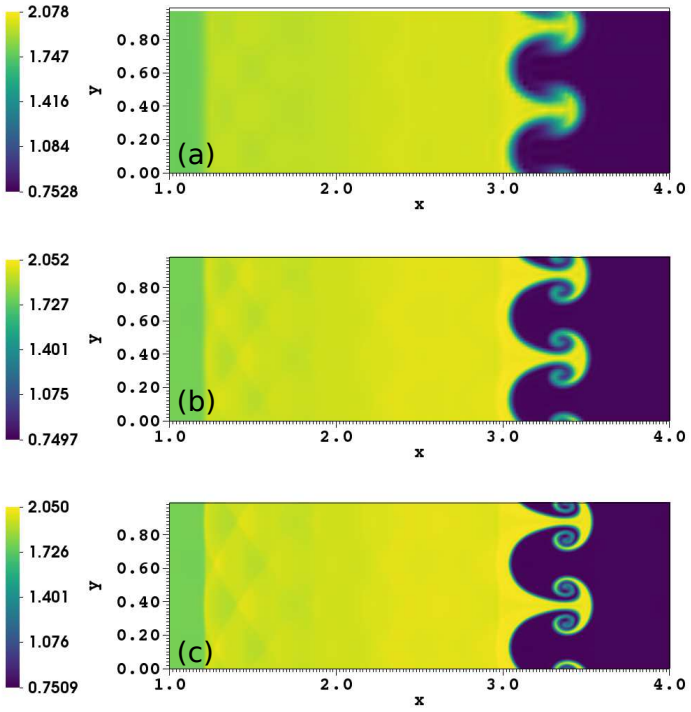

FIGURE 8. Density contours at $t = 3$ in the copper-aluminum RM problem with (a) 192×32 (b) 384×64, and (c) 768×128 grid points.

through several tests in one dimension. Robustness of the numerical method in handling material interfaces with density ratios up to 1000 is demonstrated. For quantitative validation, results of a single-material impact problem are reproduced accurately using the current multi-material algorithm. Finally, as a demonstration of the capability to simulate problems of engineering interest, two-dimensional elastic-plastic flow arising due to Richtmyer-Meshkov instability of an interface separating copper and aluminum is discussed.

Several issues need to be addressed further. Quantitative accuracy of the numerical framework needs to be established through more detailed comparisons with previously published numerical and experimental multi-material results. For this purpose, equations of state other than the separable EOS used here need to be implemented. Preliminary tests suggest that the algorithm is robust for problems involving solid-liquid or solid-gas interfaces with density/property ratios of the order of 10, although these tests are not shown here. The robustness of the algorithm to multi-phase problems, involving solid-fluid interfaces, needs to be evaluated thoroughly, followed by application to two- and three-dimensional problems of practical relevance, such as Taylor-anvil, high-velocity impact welding, and the impact and penetration of a target by a bullet.

Acknowledgments

This investigation was funded by the Lawrence Livermore National Laboratory, Department of Energy, Grant #B612155. We thank Dr. Andrew Cook for fruitful discussions, particularly related to the $p - T$ equilibrium algorithm.

REFERENCES

Achenbach, J. D. 1975 *Wave Propagation in Elastic Solids*. Elsevier.

Barton, P. T., Deiterding, R., Meiron, D. I. & Pullin, D. I. 2013 Eulerian adaptive finite-difference method for high-velocity impact and penetration problems. *J. Comput. Phys.* **240**, 76–99.

Cook, A. W. 2007 Artificial fluid properties for large-eddy simulation of compressible turbulent mixing. *Phys. Fluids* **19**, 055103.

Cook, A. W. 2009 Enthalpy diffusion in multicomponent flows. *Phys. Fluids* **21**, 055109.

Favrie, N. & Gavrilyuk, S. L. 2011 Mathematical and numerical model for nonlinear viscoplasticity. *Phil. Trans. Royal Soc. A* **369**, 2864–2880.

Favrie, N. & Gavrilyuk, S. L. 2012 Diffuse interface model for compressible fluid - compressible elastic-plastic solid interaction. *J. Comput. Phys.* **231**, 2695–2723.

Ghaisas, N. S., Subramaniam, A. & Lele, S. K. 2016 High-order Eulerian methods for elastic-plastic flow in solids and coupling with fluid flows. *AIAA Paper* 2016-3350.

Hill, D. J., Pullin, D. I., Ortiz, M. & Meiron, D. I. 2010 An Eulerian hybrid WENO centered-difference solver for elastic-plastic solids. *J. Comput. Phys.* **229**, 9053–9072.

Kawai, S., Shankar, S. K. & Lele, S. K. 2010 Assessment of localized artficial diffusivity scheme for large-eddy simulation of compressible turbulent flows. *J. Comput. Phys.* **229**, 1739–1762.

Kennedy, C. A., Carpenter, M. H. & Lewis, R. M. 2000 Low-storage, explicit Runge–Kutta schemes for the compressible Navier–Stokes equations. *App. Num. Math.* **35**, 177–219.

Lele, S. K. 1992 Compact Finite Difference Schemes with Spectral-like Resolution. *J. Comput. Phys.* **103**, 16–42.

López Ortega, A. 2013 *Simulation of Richtmyer-Meshkov flows for elastic-plastic solids in planar and converging geometries using an Eulerian framework*. Ph.D. Thesis, California Institute of Technology.

López Ortega, A., Lombardini, M., Pullin, D. I. & Meiron, D. I. 2014 Numerical simulation of elastic-plastic solid mechanics using an Eulerian stretch tensor approach and HLLD Riemann solver. *J. Comput. Phys.* **257**, 414–441.

Miller, G. H. & Colella, P. 2001 A High-Order Eulerian Godunov Method for Elastic-Plastic Flow in Solids. *J. Comput. Phys.* **167**, 131–176.

Ndanou, S., Favrie, N. & Gavrilyuk, S. L. 2015 Multi-solid multi-fluid diffuse interface model: Applications to dynamic fracture and fragmentation. *J. Comput. Phys.* **295**, 523–555.

Plohr, B. & Sharp, D. 1989 A Conservative Eulerian Formulation of the Equations for Elastic Flow. *Adv. Appl. Math.* **9**, 481–499.

Plohr, B. & Sharp, D. 1992 A Conservative Formulation for Plasticity. *Adv. Appl. Math.* **13**, 462–493.

Plohr, J. N. & Plohr, B. J. 2005 Linearized analysis of Richtmyer-Meshkov flow for elastic materials. *J. Fluid Mech.* **537**, 55–89.

Trangenstein, J. A. & Colella, P. 1991 A Higher-Order Godunov Method for Modelling Finite Deformation in Elastic-Plastic Solids. *Commun. Pur. Appl. Math.* **44**, 41–100.